Progress in PHOTOVOLTAICS

PROGRESS IN PHOTOVOLTAICS: RESEARCH AND APPLICATIONS
*Prog. Photovolt: Res. Appl.* 2015; **23**:1025–1036
Published online 13 June 2014 in Wiley Online Library (wileyonlinelibrary.com). DOI: 10.1002/pip.2523

RESEARCH ARTICLE

# Employing microsecond pulses to form laser-fired contacts in photovoltaic devices

Ashwin S. Raghavan[1], Todd A. Palmer[2]*, Katherine C. Kragh-Buetow[1], Anna C. Domask[1], Edward W. Reutzel[2], Suzanne E. Mohney[1] and Tarasankar DebRoy[1]

[1] Department of Materials Science and Engineering, Pennsylvania State University, University Park, PA 16802, USA
[2] Applied Research Laboratory, Pennsylvania State University, University Park, PA 16802, USA

## ABSTRACT

Laser-fired contacts (LFCs) are typically fabricated with nanosecond pulse durations despite the fact that extremely precise and costly control of the process is necessary to prevent significant ablation of the aluminum metallization layer. Microsecond pulse durations offer the advantage of reduced metal expulsion and can be implemented with diffractive optics to process multiple contacts simultaneously and meet production demands. In this work, the influence of changes in laser processing parameters on contact morphology, resistance, and composition when using microsecond pulses has been fully evaluated. Simulated and experimental results indicate that contacts are hemispherical or half-ellipsoidal in shape. In addition, the resolidified contact region is composed of a two-phase aluminum–silicon microstructure that grows from the single-crystal silicon wafer during resolidification. As a result, the total contact resistance is governed by the interfacial contact area for a three-dimensional contact geometry rather than the planar contact area at the aluminum–silicon interface in the passivation layer opening. The results also suggest that for two LFCs with the same size top surface diameter, the contact produced with a smaller beam size will have a 25–37% lower contact resistance, depending on the LFC diameter, because of a larger contact area at the LFC/wafer interface. Copyright © 2014 John Wiley & Sons, Ltd.

**KEYWORDS**

laser fired contact; PERC solar cell; contact resistance; microsecond pulses; laser-material interaction; three-dimensional contact

***Correspondence**

Todd A. Palmer, Applied Research Laboratory, Pennsylvania State University, University Park, PA 16802, USA.
E-mail: tap103@arl.psu.edu

Received 5 October 2013; Revised 31 March 2014; Accepted 29 April 2014

## 1. INTRODUCTION

Lasers are an important tool in photovoltaic device fabrication and are routinely used for etching [1], scribing [2], and doping [3,4]. Over the last decade, lasers have also been investigated for the processing of backside ohmic contacts on the passivated emitter rear cell structure [5–7]. Laser firing is used to create an electrical contact between an aluminum (Al) metallization layer and the bulk silicon (Si) wafer through a dielectric passivation layer [8–10]. Using this method, ohmic contacts can be fabricated without the use of photolithography and high-temperature annealing, thereby enhancing production throughput and reducing the risk of wafer breakage during high-temperature processing [11–18]. Furthermore, this approach allows devices to maintain the 22% energy conversion efficiencies observed in current passivated emitter rear cell photovoltaic devices [19] without any loss in device performance.

The majority of groups that have studied the laser-firing process have utilized single or multiple nanosecond pulses to form laser-fired contacts (LFCs) [6–11]. The drawback of nanosecond pulses is that the process leads to metal expulsion and ablation [20], which can result in a significant loss of Al at high vapor pressures and poor contact between the Al-alloyed inner crater region and the metallization across the dielectric passivation layer [21,22]. Because the alloying of Si and Al is required for proper contact formation, the depletion of Al can lead to inadequate alloying in the contacted region and low or unpredictable contact quality. The use of longer millisecond duration pulses can result in improved melting and mixing of Al and Si up to depths greater than 20 μm [23,24]. However, longer millisecond duration pulses have an adverse impact on the ability to meet production throughput requirements when LFCs are processed individually [25].

One processing timescale that has not garnered significant attention falls in the microsecond pulse length range.

With these pulse durations, contact quality may be improved by promoting the mixing of Si and Al in the contact region [7] and by enhancing the formation of a p+ local back surface field, which has been shown to decrease carrier recombination at the contact surface [8]. Furthermore, high-powered lasers, specialized beam delivery systems, and diffractive optics can be integrated to split an incoming beam into multiple beams to simultaneously process numerous contacts to meet throughput requirements [25–27]. Because clear benefits can be associated with microsecond pulse durations, it is critical to evaluate how LFCs form within this processing regime and the resulting impact on electronic properties.

In this research, LFCs are produced using microsecond pulse durations and a 1070 nm wavelength laser over a wide range of laser fluences. Comprehensive materials characterization is performed to evaluate how changes in laser processing parameters impact LFC morphology, alloying of the Al and Si within the laser-affected region, and total contact resistance. LFC cross-sections obtained via focused ion beam (FIB) milling are used to develop an understanding of the impact that laser firing has on the Si crystal lattice, the size of the opening in the passivation layer, and the overall contact geometry. The LFC geometries are revealed to be three-dimensional with a two-phase Al–Si microstructure within the resolidified region. The impact that the three-dimensional contact geometry has on total contact resistance is explained using carrier transport simulations. By comparing experimental contact resistance measurements with the simulated results, it is demonstrated that the spreading resistance calculated by the Cox–Strack relationship for a planar interfacial contact area is not accurate when considering the hemispherical and half-ellipsoidal three-dimensional contact geometries formed using microsecond pulse durations.

## 2. EXPERIMENTAL PROCEDURE

In order to characterize the LFC formation process when using microsecond pulses, 500-μm-thick, 9 Ω-cm resistivity, double side polished, <100>, p-type, float zone, crystalline Si wafers were used. The front sides of the wafers were passivated with 100 nm of $SiO_2$ via plasma-enhanced chemical vapor deposition using a $SiCl_3/O_2/Ar$ gas mixture in an Applied Materials P5000 system. Next, approximately 2- and 0.4-μm-thick Al layers were sputtered on the front and backside, respectively, using a Denton DV-502A DC magnetron sputtering tool at a base pressure less than $1 \times 10^{-7}$ Torr at a rate of 0.1 to 0.2 nm/s. Prior to laser processing, electrically isolated regions (1.5 mm × 1.5 mm area) were created with lift-off on the front side using contact photolithography. Individual LFCs were processed on each insulated pad. Figure 1 shows a schematic diagram of the substrate configuration used for laser firing.

An IPG Photonics® (Oxford, MA, USA) YLR-LP Series 1070 nm single-mode fiber laser that emits in the $TEM_{00}$ mode with 500 W maximum power was used for processing.

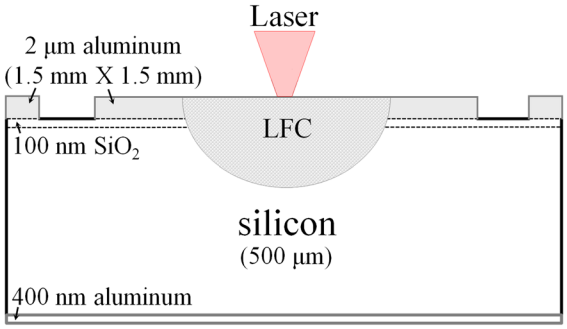


**Figure 1.** Schematic diagram of experimental substrate used for laser-fired contact (LFC) investigation.

Using laser power levels between 112 and 460 W and pulse durations ranging from 20 to 100 μs, fluence levels were varied by changing the laser beam diameter from 50 to 70 μm. Laser firing was performed using the laser powers and pulse durations shown in Tables I and II with fluences ranging from 58 to 2343 J/cm$^2$/pulse. Pulse durations were modulated using a control system programmed with the National Instruments LABVIEW® software (Austin, TX, USA). Pulse durations were confirmed via oscilloscope readings from a Newport (Irvine, CA, USA) 818-BB-21 high-speed photodiode.

Laser-fired contacts were characterized using a number of techniques to evaluate the laser–material interaction

**Table I.** Measured total contact resistances (Ω) with processing parameters for 50 μm beam diameter.

| | Power (W) | | | | |
|---|---|---|---|---|---|
| Time (μs) | 112 | 159 | 260 | 360 | 460 |
| 20 | NC | NC | 582 | 477 | 498 |
| 30 | NC | 1097 | 347 | 288 | 348 |
| 40 | NC | 595 | 266 | 297 | 271 |
| 50 | 1183 | 358 | 284 | 263 | 206 |
| 75 | 668 | 296 | 241 | 223 | — |
| 100 | 361 | 263 | 233 | 204 | 172 |

NC, no contact formed.
[a]No data available for 460 W, 75 μs.

**Table II.** Measured total contact resistances (Ω) with processing parameters for 70 μm beam diameter.

| | Power (W) | | | | | |
|---|---|---|---|---|---|---|
| Time (μs) | 159 | 210 | 260 | 312 | 360 | 460 |
| 20 | NC | NC | NC | NC | 482 | 437 |
| 30 | NC | 783 | 469 | 393 | 292 | — |
| 40 | 1315 | 528 | 410 | 293 | 273 | — |
| 50 | 573 | 432 | 318 | 283 | 265 | 212 |
| 100 | 622 | 260 | 222 | 208 | 184 | 126 |

NC, no contact formed.
[a]No data available for 460 W, 30 and 40 μs.

behavior, LFC fusion zone, passivation quality, and electrical resistance. Contact morphology was determined from images obtained using an FEI (Hillsboro, OR, USA) Quanta 200 environmental scanning electron microscope (SEM). Using the same system, elemental concentrations of Al and Si on the surface were measured by electron dispersive spectroscopy (EDS) using a 5 keV accelerating voltage and 1 μm beam size. Samples were cross-sectioned close to the contact centerline with an ADT (Yokneam, Israel) 7100 ProVectus dicing saw, and the cross-sections were polished using an FEI Quanta 200 3D dual beam FIB. Prior to polishing, a carbon or platinum coating was deposited on the surface of the sample near the face to be polished to protect the edge from deteriorating during the milling process. For FIB samples, SEM imaging and EDS mapping were performed using an FEI NanoSEM 630 field emission SEM and analyzed using the Oxford (Abingdon, England) AZTEC software.

The surface topography of the contacts was determined by optical profilometry using a ZYGO (Middlefield, CT, USA) NewView™ 7300 optical profilometer and its accompanying METROPRO® version 8.3.5 software. Total contact resistance was measured with a probe station and a Keithley (Cleveland, OH, USA) 4200 semiconductor characterization system using four probes to eliminate the resistance contribution from the wiring and probes. The total resistance between three pairs of electrically insulated contacts was measured from the front side of the wafer. Using the measured resistances for the three pairings, each individual contact resistance was back calculated by simultaneously solving a system of three equations. Calculated contact resistances were reproducible with less than 10% variation when different contact pairings were used.

# 3. RESULTS AND DISCUSSION

## 3.1. Contact morphology

The impact of changing laser processing parameters on contact morphology was evaluated using scanning electron microscopy and optical profilometry. Figure 2 shows SEM images of the top surface and the corresponding surface contour maps for two contacts produced using a 50 μm beam diameter. The contact in Figure 2(a) was produced with 160 W laser power and a 30 μs pulse, corresponding to a fluence of 244 J/cm$^2$. The contact in Figure 2(b) was produced with 260 W laser power and a 40 μs pulse, corresponding to a fluence of 530 J/cm$^2$. The lower fluence value is the threshold at which an ohmic contact with a measureable electrical resistance of 1097 Ω was formed with no melt displacement, while the higher fluence value represents the threshold at which an ohmic contact with a resistance of 582 Ω was formed and marked melt displacement occurred (as seen in Figure 2). In all cases where laser-fired Al–Si ohmic contacts were formed when using microsecond pulse durations, the contacts exhibited a distinct inner crater and outer ring, as noted in Figure 2.

For the experiments run, the output beam from the fiber laser used has a Gaussian irradiance (or laser power per unit area) distribution, $F$, emitting in the $TEM_{00}$ mode that can be calculated using the following equation:

$$F = \frac{qf\eta}{\pi r^2} e^{-f^{(x^2+y^2)}/r^2} \quad (1)$$

where $q$ is the laser power, $f$ is the distribution factor (taken here as 3 to accurately simulate the output from the fiber

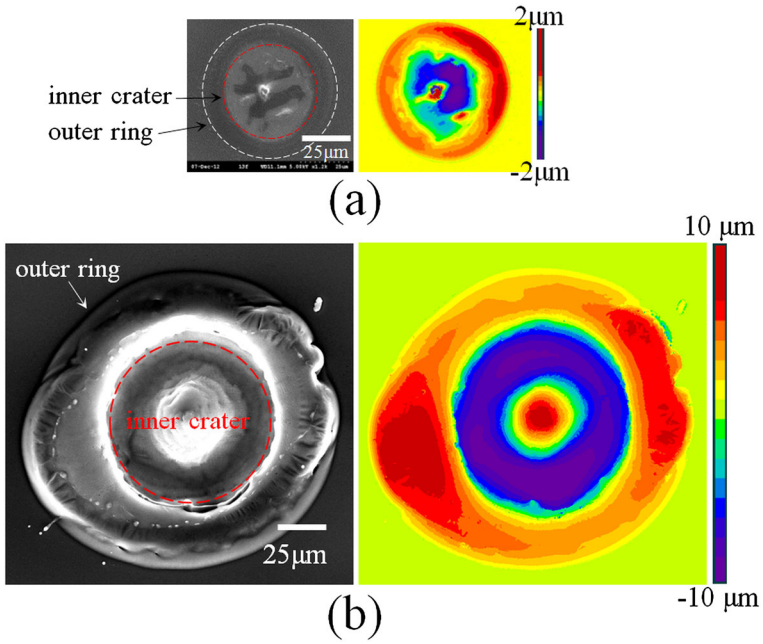


**Figure 2.** Scanning electron microscope micrographs and optical profilometry measurements for laser-fired contacts processed with 50 μm beam diameter using (a) 160 W laser power and 30 μs pulse length and (b) 260 W laser power and 40 μs pulse length.

laser [7]), $\eta$ is the absorptivity of the laser wavelength at the substrate surface, $r$ is the beam radius, and $x$ and $y$ are the distances from the beam center. From Equation (1), it can be seen that the intensity of the laser radiation will be highest in the center. The inner crater region forms where the material first melts under laser irradiation and grows radially with time based on conductive and convective heat transfer mechanisms, which will be highly dependent on pulse length and power level. This inner crater region will grow in size with increasing fluence as seen in Figure 2. The formation of the outer ring region, however, is caused by ejection of Al and Si from the inner crater region at higher fluences.

Using higher fluence will cause the substrate surface temperature to increase more rapidly than lower fluences. The rate at which the temperature increases depends on a number of factors, such as the relative concentration of alloying elements within the melt [21] and the laser wavelength absorption coefficient of the material [7]. As the molten pool surface temperatures increases, the vapor recoil pressure on the surface of the melt pool will increase as the alloying elements are vaporized. For molten material to escape the melt region, the recoil pressure of the melt flow must exceed the surface tension pressure at the periphery of the melt pool [28]. By increasing the fluence from 244 to 530 J/cm$^2$ for the contacts shown in Figure 2, the recoil pressure on the surface leads to pronounced melt displacement from the molten pool center and the formation of an outer ring because of recoil pressure driven outward flow.

Figure 3 shows surface deformation profiles measured via optical profilometry through the center of various contacts as a function of pulse duration and laser beam diameter with an average laser power of 260 W. The deformation profiles in Figure 3(a) were processed with a 50 μm beam diameter, whereas the profiles in Figure 3(b) were obtained when processing with a 70 μm beam diameter. In all cases shown in Figure 3 (except for the contact

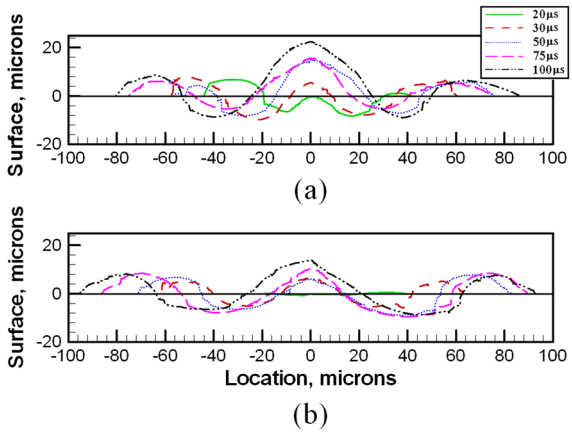


**Figure 3.** Surface deformation with respect to the original surface of the aluminum metallization layer as a function of time and power density when processing with 260 W laser power and (a) 50 and (b) 70 μm beam diameters.

processed with a 70 μm beam diameter and a 20 μs pulse), a central peak forms within the inner crater and grows monotonically as a function of increasing pulse duration, which will also correspond to an increase in the fluence. There are two possible explanations for the formation of this peak. Previous work on laser texturing of Ni–P magnetic disk substrates using nanosecond pulses has demonstrated that the central peak is due to a competition between the surface tension gradient driven Marangoni flow and the compositional gradient driven flow [29]. The depletion of a surface active element, such as oxygen or phosphorus, can cause the transient shear stress on the molten pool surface to be negative, which will induce a radially inward force on the melt causing the central peak during solidification.

For our work, however, the central peak effect is more pronounced (approximately 2 orders of magnitude larger in height) than those formed with nanosecond pulses owing to higher fluences, longer pulse durations, and slower cooling rates during solidification. In Figure 3(a), it can be observed that when increasing the pulse length from 30 to 100 μs for a 50 μm beam diameter, the central peak height increases from 4 to 21 μm. When using a 70 μm beam diameter and a 100 μs pulse, the central peak is approximately 17 μm. On the basis of the size of the central peaks formed here, an alternative explanation for the peak formation is that with increasing fluence, the recoil pressure will be larger, along with the potential energy stored in the depressed melt pool surface. When the evaporative vapor recoil pressure is removed at the termination of the laser pulse, the surface will rebound and form a central peak upon solidification.

Figure 4(a) and (b) shows the inner crater size as a function of pulse duration and laser power for beam diameters of 50 and 70 μm, respectively. In both cases, the inner crater contact size increases with longer pulse durations and increasing laser power. Because the pulse lengths are still sufficiently short that the process has not yet reached steady state, the molten pool peak temperatures will rise rapidly throughout the laser-firing process. As a result, there will be an increasing Marangoni shear stress on the surface driven by the large temperature gradients, and the size of the contacts will grow rapidly because of increasing fluid flow velocities and convective heat transfer from the center to the periphery of the molten pool [7,21]. Figure 4 (a) shows that when using a 50 μm beam diameter, increasing the laser power from 160 to 460 W leads to an increase in the inner crater diameter of approximately 40 μm at each pulse length. LFCs processed with a 70 μm beam diameter, however, exhibit larger inner crater sizes when using the same laser beam power and pulse duration, as shown in Figure 4(b). It is likely that when using a larger beam size, the melting threshold for both Al and Si is reached at larger distances away from the beam center than when using a smaller beam size. Therefore, the inner crater size is larger despite the fact that the smaller beam size will have higher peak temperatures and higher fluid flow velocities within the melt.

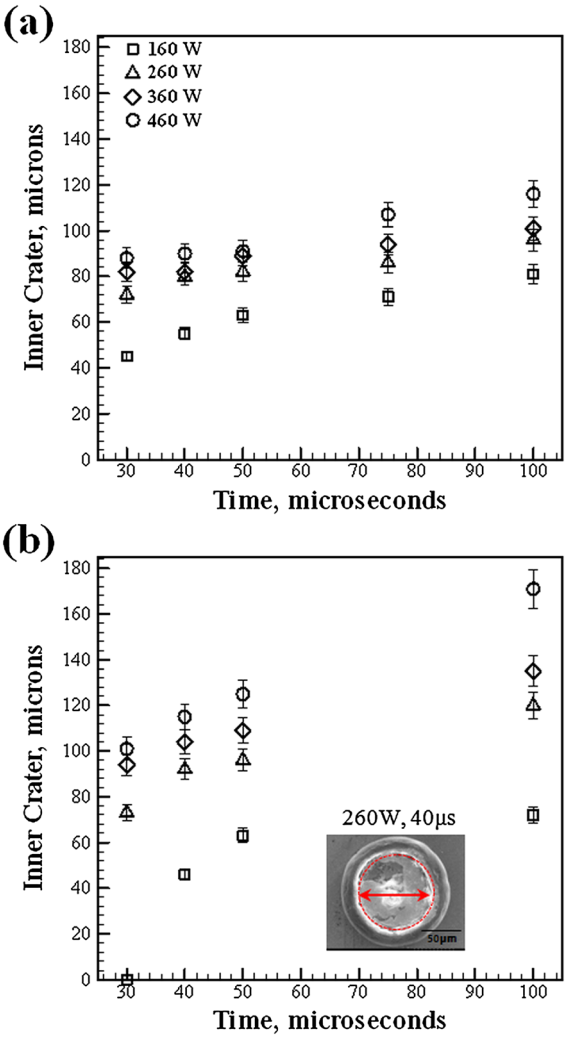


**Figure 4.** Inner crater contact size as a function of pulse length and power level for (a) 50 and (b) 70 µm beam diameters.

Although the contacts processed with a smaller beam diameter have smaller inner diameters, they should have larger depths of penetration because the spatial variation of the power density distribution across the surface of the melt as calculated by Equation (1) will be substantially higher when using a small beam diameter. It has been shown through numerical simulations of the LFC process [7] that when two contacts have the same top surface area, the one processed with a smaller beam diameter will have a larger depth of penetration because the laser intensity at the center of the beam will be higher leading to greater heat transfer by convection and conduction. As the irradiance increases through a reduction in beam size, the mode of laser processing will eventually transition from conduction mode to keyhole mode [30], and the shape of the molten volume will change from hemispherical to ellipsoidal with large penetration depths. Understanding the influence that changes in laser parameters have on contact geometry and the resulting total contact resistance is important in order to optimize the LFC process.

### 3.2. Electrical characterization

The total measured contact resistance, $R_{LFC}$, is related to the spreading resistance, $R_S$, and the individual contact resistance, $R_C$ [17]. The total LFC resistance is calculated as follows:

$$R_{LFC} = R_S + R_C \tag{2}$$

The spreading resistance for an LFC processed with nanosecond pulse lengths is typically calculated using the Cox–Strack relationship for a planar, two-dimensional contact [31]:

$$R_S \cong \frac{\rho_b}{2\pi r} arctan\left(\frac{2W}{r}\right) \tag{3}$$

where $\rho_b$ is the base resistivity, $r$ is the contact radius, and $W$ is the wafer thickness. The individual contact resistance is calculated as follows:

$$R_C \cong \frac{\rho_{cef}}{\pi r^2} \tag{4}$$

where $\rho_{cef}$ is the effective specific contact resistance ($\Omega$-cm$^2$). The value of $R_{LFC}$ should approach the spreading resistance as the contact quality improves and the contribution from the specific contact resistance at the Al/Si interface becomes negligible. An increase in the inner crater size, which is the location where there is an opening in the passivation layer and the Al has alloyed with the Si [14], has been shown to lead to a reduction in total contact resistance for nanosecond pulses based on a reduction in the spreading resistance per Equation (3) [17].

For the range of laser power and pulse durations used in this study, the influence of LFC inner crater size on total contact resistance is plotted in Figure 5. In addition, the spreading resistance as calculated by the Cox–Strack equation is plotted for a base resistivity of 9 $\Omega$-cm. The individual contact resistance, $R_c$, is not considered and assumed negligible based on the extremely low contact resistivities of $4 \times 10^{-6}$ $\Omega$-cm$^2$ for Si heavily doped with Al [32]. For an LFC with a 50 µm radius, this corresponds to a resistance of 0.02 $\Omega$, which is much lower than the measured values. Processing parameters are shown in Tables I and II for 50 and 70 µm beam diameters, respectively, along with the measured total contact resistances. The data represents the average measured resistance value as determined from multiple measurements in which the standard error (calculated as the standard deviation divided by the mean) was no more than 10%.

From Figure 5, it can be clearly observed that the Cox–Strack relationship for a planar contact drastically overpredicts the total contact resistance when increasing contact diameters. It can also be observed that as the LFC

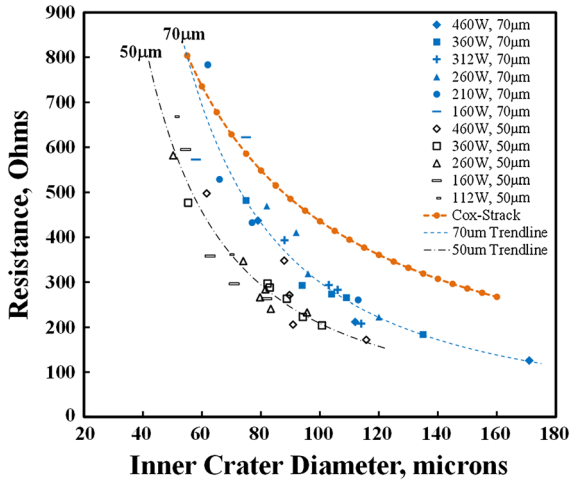


**Figure 5.** Total contact resistance as a function of inner crater diameter, laser power, pulse duration, and laser beam diameter. Trendlines for 50 and 70 µm beam diameters are included for clarity.

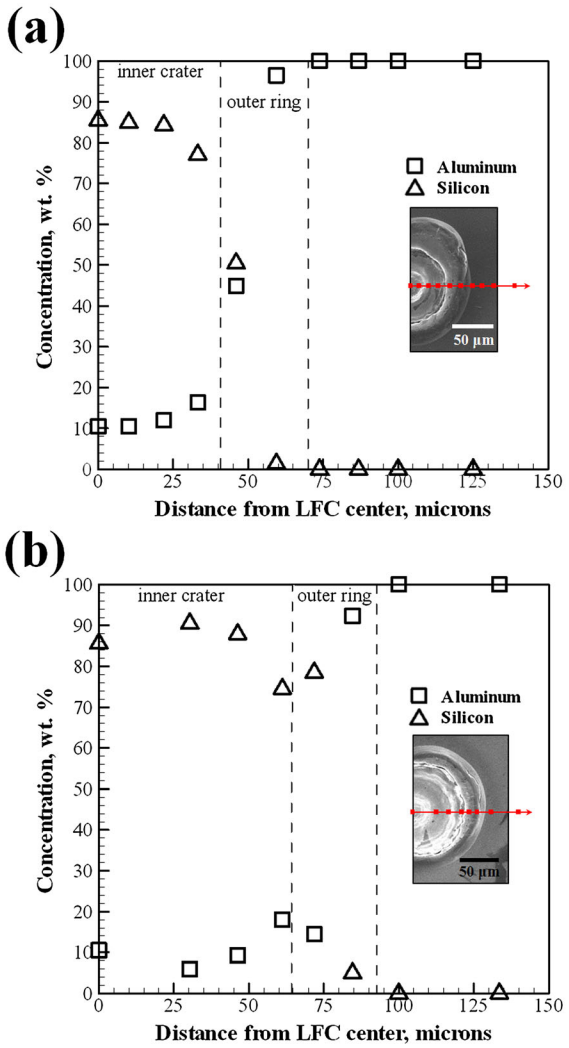


**Figure 6.** Electron dispersive spectroscopy measurements along top surface for (a) 260 W, 50 µs pulse, and 50 µm beam diameter (662 J/cm2 peak fluence and 284 Ω total contact resistance) and (b) 360 W, 40 µs pulse, and 70 µm beam diameter (374 J/cm2 peak fluence and 273 Ω total contact resistance). The insets show the locations of the measurements for the specific contact.

inner crater diameter increases, the total contact resistance decreases when using either a 50 or a 70 µm beam diameter. Although the trend is the same regardless of beam size, a change in the beam diameter has a noticeable impact on the measured total contact resistance for two contacts with the same inner crater diameter. Specifically, the total contact resistance can be significantly lower for the same inner crater diameter when using the smaller 50 µm beam diameter. For instance, for an inner crater diameter of 100 µm, the contact resistance is approximately 220 Ω when using a 50 µm beam diameter, whereas it is nearly 330 Ω when using a 70 µm beam diameter. Because there is a clear difference observed in the total contact resistance despite an identical inner crater size, the results suggest that the contact area is governed by a larger region than the inner crater. In order to evaluate how a change in beam diameter resulted in varying total contact resistance despite having the same inner crater size, the composition along the top surface was measured to determine if detectable changes in Al and Si concentration influence contact formation.

Figure 6 shows results for EDS traces taken across the surface of two solidified LFCs from the center of the contact to the unaffected Al metallization. In order to assess the depth of elemental detection for the measurement technique, the anticipated electron trajectories and spatial resolution for the EDS signal were evaluated using Monte Carlo Casino [33] simulations for the substrate configuration shown in Figure 1 and known electron beam parameters. The results suggest that detection will be within 300 nm from the surface over the 1 µm beam size, giving good spatial resolution considering the size of the contacts. The inner crater region and outer ring region are delineated on the plots based on the inset SEM micrograph. Figure 6 (a) shows the EDS results for a contact processed with 260 W laser power, a 50 µs pulse, and a 50 µm beam diameter (662 J/cm$^2$ fluence). The EDS trace confirms the presence of Al and Si within the inner crater. In addition, Al and Si are detected throughout the outer ring. The results show only Al within the unprocessed metallization layer. Figure 6(b) shows a contact processed with 360 W laser power, a 40 µs pulse, and a 70 µm beam diameter (374 J/cm$^2$ fluence). In this case, Al and Si are detected within the inner crater and outer ring as well. The presence of Al and Si in the outer ring suggests that material is being expelled from the inner crater region during processing mainly because of large vapor recoil pressures on the surface of the melt pool. Because these are single-line EDS scans, a more thorough examination of the LFC cross-section is required to determine how uniformly Al is distributed within the contact.


DOI: 10.1002/pip

In order to further evaluate how Al is distributed within the LFC and outer ring, a sample was cross-sectioned using a dicing saw and polished using a FIB. Figure 7(a) shows a cross-section of an LFC processed with 260 W laser power, a 40 µs pulse, and a 70 µm beam diameter (270 J/cm$^2$). From the SEM image in Figure 7(a) at a tilt of 44°, a faintly visible fusion line can be seen along certain regions around the melt (shown with the arrows and red line on the right-hand side). This region represents where the Si single-crystal base material has melted and mixed with Al and recrystallized during solidification. A plane view of the cross-section can be seen in Figure 7(b) in which recrystallization of the Si because of the presence of Al can be observed within the fusion zone on the left-hand side of the contact. EDS maps in Figure 7(c) and (d) shows the distribution of Al and Si, respectively, within the recrystallized material. In these figures, the Al metallization layer outside the contact area was unintentionally removed by the dicing saw during sample preparation. As a result, Al is not present along the top surface of the sample outside of the LFC in Figure 7(c).

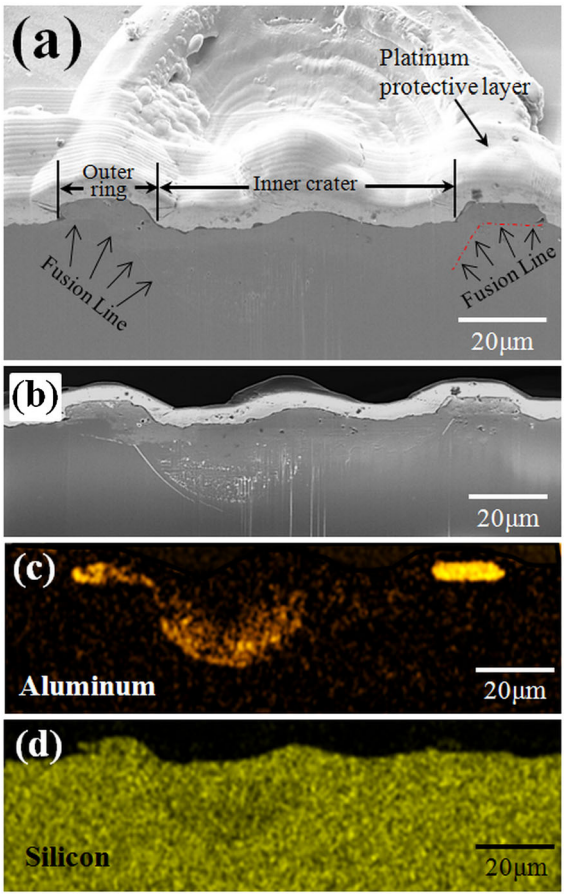


**Figure 7.** Focused ion beam polished scanning electron microscope cross-section for laser-fired contact processed with 260 W laser power, 30 µs pulse length and 70 µm beam diameter (202 J/cm2 peak fluence with 469 Ω total contact resistance) at (a) 44° tilt and (b) no tilt. Electron dispersive spectroscopy maps for (c) aluminum series (no tilt) and (d) silicon (no tilt). Faintly visible fusion line indicated with red line on right-hand side.

Figure 7(c) shows a higher concentration of Al within the left-hand side inner crater region. The outer ring region also shows the presence of Al on both sides and is substantially brighter on the right-hand side, indicating a higher concentration of Al. This additional Al was most likely displaced from the inner crater at the onset of processing and not adequately incorporated into the melt. The irregularity in the mixing suggests that the beam may not have been perfectly Gaussian, leading to nonuniform heating of the substrate despite a circular beam. On the left-hand side, Al has clearly mixed throughout the melt, which is likely because of convective mass transfer of the Al as has been shown for laser doping of Si with phosphorus [34]. Because of surface tension gradient driven Marangoni flow for Si, molten material will flow along the surface from the high-temperature center region to the low-temperature periphery before returning to the center through the depth of the melt [7,35]. These flow patterns will lead to convective mixing of the Al in the molten Si, which is observed in Figure 7(c), in which Al is detected at a depth of approximately 25 µm. The EDS map for Si in Figure 7(d) shows Si throughout the melted region and also within parts of the outer ring.

Figure 8 shows additional FIB cross-sections for two contacts fabricated with 112 W laser power, a 50 µm beam diameter, and pulse lengths of (a) 50 and (b)/(c) 100 µs. The total contact resistances measured were 1183 Ω and 361 Ω for the 50 and 100 µs pulses, respectively. Figure 8 (a), which is a micrograph for the contact processed with a 50 µs pulse and a fluence of 285 J/cm$^2$, shows that the opening in the passivation layer is only present within the inner crater region. The presence of the passivation below the outer ring suggests that the total contact area is not impacted by this region despite the presence of Al and Si on the surface. Voids in the crystalline Si are observed near the openings in the passivation on both sides of the inner crater, which are likely caused by rapid interdiffusion of Si into the Al metallization.

Within the inner crater region where there is an opening in the passivation layer, the presence of a two-phase Al and Si microstructure can be observed. One such region is highlighted in the red box in Figure 8(a) and is enlarged in Figure 9. Figure 9 shows the presence of both Al (green) and Si (blue) within the inner crater region. Despite the clear interdiffusion of Al and Si seen in Figure 9, the total contact resistance is extremely high (1183 Ω). This unexpectedly high contact resistance may be because the heavily doped Al region is not uniform throughout the cross-section as seen in Figure 8(a). Nonuniform heating by the laser beam and/or other competing processes involved in the initiation of contact formation, such as the melting of the passivation layer, may be the cause.

Figure 8(b) and (c) shows FIB cross-sections from different regions within a contact processed with a 100 µs pulse and a higher fluence of 570 J/cm$^2$ and that exhibits a much lower resistance (361 Ω) and larger inner crater


DOI: 10.1002/pip

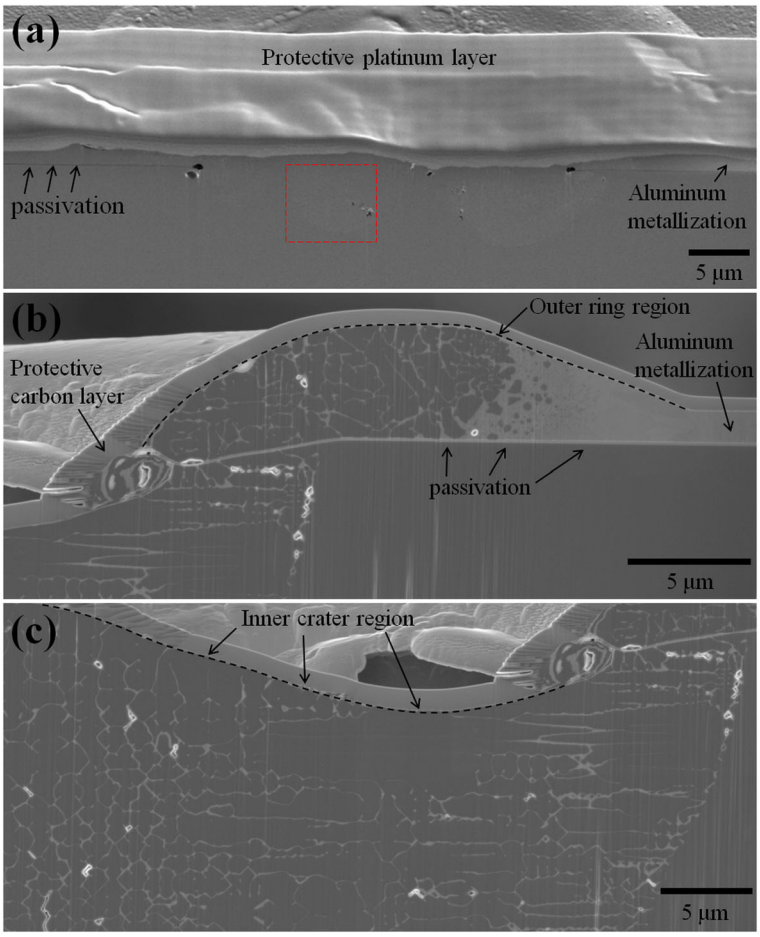


**Figure 8.** Scanning electron microscope micrographs of cross-section for contacts processed with 112 W laser power, a 50 μm beam diameter, and (a) 50 μs pulse (resistance of 1183 Ω) and (b) and (c) 100 μs pulse duration (resistance of 361 Ω) where (b) is below the outer ring and (c) is toward center of the laser-fired contact. Red box in (a) is enlarged in subsequent figure.

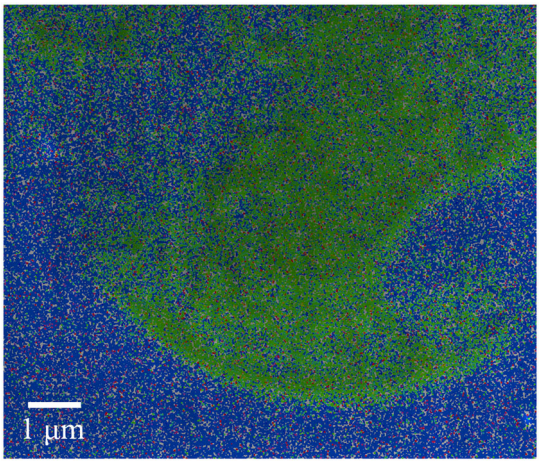


**Figure 9.** Electron dispersive spectroscopy map for boxed region in Figure 8(a) shows diffusion of aluminum (green) and silicon (blue) during contact formation when processing with 112 W laser power, a 50 μs pulse length, and a 50 μm beam diameter.

size. Figure 8(b) shows the right side of the contact region near the passivation layer, further confirming that the passivation layer remains intact below the outer ring region even at higher fluences. Within the cross-sections, the white region represents a second phase with higher concentration of Al, and the darker region is the Si-rich phase. At this higher fluence level, it can be observed that some of the Al was expelled during processing and solidified on the surface within the periphery of the outer ring without completely mixing with the Si. Because the melting point of pure Al is 933 K and the boiling point is 2792 K versus 1687 and 3514 K for Si, respectively, metal expulsion of the Al layer will initiate prior to substantial melting of the Si and/or formation of an Al–Si eutectic.

Closer toward the inner crater region, however, Al is well mixed with the Si within the outer ring as seen in Figure 8(b). Because of the mixing of Al and Si within this region, a two-phase Al–Si microstructure forms. Furthermore, the solidification process will undergo nonequilibrium cooling that will influence the resulting microstructure because of rapid cooling cycles associated


*Prog. Photovolt: Res. Appl.* 2015; **23**:1025–1036 © 2014 John Wiley & Sons, Ltd.
DOI: 10.1002/pip

with laser processing [7]. Figure 8(c) shows a large portion of the inner crater region for the same contact shown in Figure 8(b). A similar two-phase microstructure can be observed in this region. Because of the variation in thermal cycles within the molten region associated with laser processing of LFCs [7], the solidification structure varies within the melt region from the fusion boundary to the center of the melt. The solidification morphologies vary from more cellular growth closer to the fusion line to a more equiaxed dendritic structure at the center of the contact. The change in solidification morphologies has been observed in similar studies of laser spot welding [35] and is primarily driven by the temperature gradient at the interface between the liquid and the two-phase Al–Si region and the growth rate of the liquid/two-phase solidification front. The variation in solidification behavior will be influenced by the selection of laser processing parameters.

Additional imaging performed using an ion beam revealed absolutely no contrast in the various crystalline substructures shown in Figures 7 and 8, suggesting that the resolidification occurs as a single crystal because of epitaxial growth. Similar behavior has also been observed in high energy density welding of single-crystal nickel-based alloys [36]. The solidification substructures (i.e., dendrites and cells) will, however, possess different orientations based on the preferential growth directions of the solidifying melt pool from the fusion boundary of the contact [36]. In both cases where high and low resistances were produced in Figure 8 by varying fluence, the contacts exhibited areas where Al was incorporated into the Si well beyond the planar Al–Si interface area at the opening in the passivation layer. The presence of Al at large depths within the resolidified Si will result in a contact that is not planar in shape, and may be the primary contributor to the differences in the total contact resistances observed in Figure 5 when using different laser beam diameters despite having the same LFC top surface diameter.

### 3.3. Total contact resistance simulations

The influence of a three-dimensional contact geometry on total contact resistance was explored through modeling of the carrier transport by self-consistently solving Poisson's equation and the carrier continuity equation with drift-diffusion physics using the commercial software SENTAURUS by Synopsys, Inc. (Mountain View, CA, USA). Simulations were performed using a two-dimensional rectangular computational domain that was 500 μm thick based on the wafer thickness, and the length was equal to three times the thickness. The total contact resistances were then calculated for three-dimensional geometries using cylindrical symmetry. The substrate was modeled as doped p-type Si with a boron acceptor concentration of $1.5\times10^{15}\,\mathrm{cm}^{-3}$ [37] based on the known wafer base resistivity of 9 Ω-cm. The individual contact resistance, $R_C$, was assumed to be negligible because of the extremely low specific contact resistances on the order of $4\times10^{-6}\,\Omega\text{-cm}^2$ known for Si very heavily doped with Al [32]. Simulations were performed assuming Al dopant densities of $2\times10^{19}\,\mathrm{cm}^{-3}$ based on experimental data for Al concentration in Si annealed at 800 °C [38]. Total contact resistance was determined from the slope of voltage/current plots that were generated for a dc bias of 0–2 V between the top surface of the LFC with the bottom surface at ground.

Contacts were modeled in two-dimensions as semicircles and half-ellipses (as shown in the inset in Figure 10) with a contact diameter, $a$, and a contact depth, $c$, because previous heat transfer and fluid flow modeling of the transient growth of the LFC geometry has revealed that contacts when processed with microsecond pulses will be hemispheres or half-ellipsoids [7]. For example, the heat transfer and fluid flow model revealed that a reduction in beam diameter by approximately 20 μm caused the depth of penetration to increase by 1.5 times for the power levels considered in that study, which would cause the LFC shape to change from a hemisphere to a half-ellipsoid. The contact diameter, $a$, was selected on the basis of the values obtained from the experimental measurements for inner crater LFC diameter shown in Figure 5. For the ellipses, the depth, $c$, was taken as the same length as the contact diameter ($c=a$) to account for the change in penetration depth when processing with a smaller beam size.

Figure 10 shows a plot of the total contact resistance for the experimental and simulated results as a function of the inner crater LFC diameter. In order to clearly distinguish the simulated results from the experimental results, experimental measurements are plotted as data points based on the trendlines shown in Figure 5 for the total contact resistance data for 50 and 70 μm beam diameters. When looking at the simulated contacts resistances for the hemispheres and the half-ellipsoids, it is clear that despite the fact that the inner crater LFC diameter is the same size, the total contact resistance is different. For instance, when

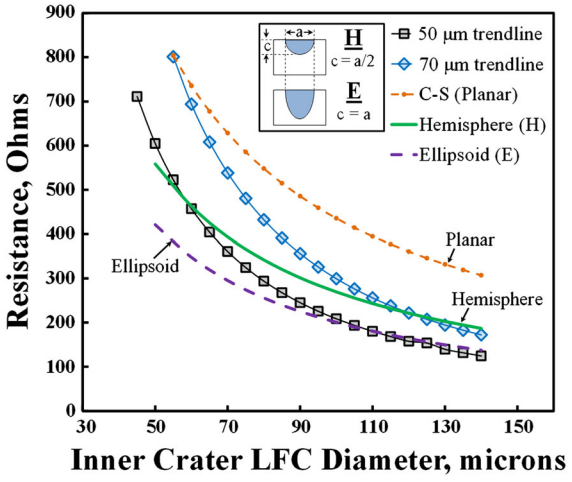


**Figure 10.** Device simulations for total contact resistance assuming hemispherical or half-ellipsoidal contact shape (with Al doping concentration of $2\times10^{19}\,\mathrm{cm}^{-3}$) versus planar Cox–Strack (C-S) calculation per Equation (3) and measured experimental values for microsecond pulse laser-fired contacts (LFCs).

the diameter is 90 μm, the contact resistance is 225 Ω for the half-ellipsoid versus 301 Ω for the hemisphere. Because the half-ellipsoid has a larger contact area at the LFC/wafer interface, the calculated spreading resistance is nearly 25% less, which explains the shift in the curves for the simulations when modeling a hemisphere versus half-ellipsoid.

The experimental total contact resistance data when processing with the 70 μm beam starts close to the planar approximation by the Cox–Strack equation but deviates rapidly and approaches the values predicted for the hemisphere. Heat transfer and fluid flow modeling of the transient growth of LFCs when using microsecond pulse lengths support the idea that the contact will start off more planar but take on a more three-dimensional shape with increasing processing time [7]. At the onset of processing, the contacts processed with the larger beam will be more elliptical in shape with the depth, *c*, being much smaller than the inner crater LFC diameter, *a*. Therefore, the resistance will be better predicted by a planar approximation. However, as the contact grows in size either by increasing laser power or through the use of longer pulse durations, the contact size will continue to grow into a hemispherical shape, and the *c/a* ratio will increase from 0 to 0.5. As this occurs, the experimental data approaches the simulated data for total contact resistance of a hemisphere. This LFC shape has also been observed through heat transfer and fluid flow simulations in which it was shown that when processing with 25 W laser power and a 20 μm beam diameter, the *c/a* ratio was 0.2 after 1 μs and reached 0.43 by 30 μs.

Similarly, the contacts processed with the 50 μm beam diameter will take on a hemispherical shape more quickly because of the concentrated power density distribution predicted by Equation (1). As the duration of the laser pulse increases, the depth of penetration will increase and the *c/a* ratio will increase greater than 0.5. When the *c/a* ratio reaches 1, which corresponds to the simulated data for the half-ellipsoid shown, there is good agreement in total contact resistance between the experiments and simulations. Therefore, for two contacts processed with a different beam diameter yet possess the same top surface LFC inner crater diameter, it can be expected that the penetration depth will be larger for the contact processed with the smaller beam size, and total contact resistance will be lower. With a larger penetration depth yet similar top surface inner crater diameter, the contact area at the LFC/wafer interface will be greater for the contact processed with the smaller beam. As a result, we observe the shift in curves observed in Figure 5 when looking only at the top surface inner crater diameter.

The total contact resistance for LFCs processed with nanosecond pulse durations is best approximated by the empirical Cox–Strack relationship for planar contacts [17]. For the contacts produced with the microsecond pulse durations, the total contact resistance is significantly lower and also depends on the contact geometry produced (i.e., half-ellipsoidal or hemispherical). When comparing the contact resistances presented in Figure 10 for planar and three-dimensional contacts, it can be observed that the total contact resistance is approximately 37% and 53% less than that predicted for planar contacts over the entire range of top surface LFC diameters for hemispherical and half-ellipsoidal contacts, respectively. For example, the total contact resistance for an LFC diameter of 80 μm is 541 Ω for a planar contact in comparison to 342 Ω for a hemispherical contact and 256 Ω for a half-ellipsoidal contact. Therefore, significant reductions in individual contact resistance can be achieved by employing three-dimensional contacts.

It is also worth noting that with these processing conditions, the simulated data for the hemispheres and half-ellipsoids suggest that recrystallization depths with Al alloying greater than 100 μm can be achieved. Therefore, because the passivation layer remains intact outside of the inner crater region (as seen in Figure 8), it is possible that the larger contacts may improve carrier collection because photogenerated carriers would not have to travel as far to reach the LFC. However, a contact that occupies a larger volume would reduce the available volume of Si for the photogeneration of carriers. Because these phenomena are at odds, it is important to experimentally quantify the impact on device efficiency. Nevertheless, on the basis of the good agreement between the experiments and simulations for total contact resistance as a function of inner crater LFC diameter, it is clear that to obtain the lowest total contact resistance, laser processing parameters should be carefully selected when using microsecond pulse lengths to optimize the *c/a* ratio while maximizing the area at the LFC/wafer interface without damaging the wafer

## 4. SUMMARY AND CONCLUSIONS

The use of microsecond pulses to form LFCs was comprehensively evaluated through characterization of surface morphology, contact geometry, concentration, and total contact resistance as a function of laser processing parameters. From the results, the following conclusions can be made:

(i) The contact size for LFCs processed with microsecond pulse lengths is governed by the contact area at the three-dimensional LFC/wafer interface rather than the planar LFC contact area at the Al–Si interface through dielectric passivation layer. As a result, the total contact resistance is dependent on the surface area of the molten region with dissolved Al, which will be hemispherical or half-ellipsoidal depending on the laser parameters used.
(ii) The opening in the passivation layer is restricted to the region designated as the inner crater LFC diameter. An outer ring forms because of metal expulsion based on the laser beam energy density. However, the passivation layer remains largely intact below this region. In addition, the Al that is


DOI: 10.1002/pip

not expelled from the melt region during processing mixes with the Si to form a two-phase microstructure. The presence of Al leads to heavy doping of the p+–Si and contributes to reducing the total contact resistance.

(iii) Using a smaller beam diameter to produce a contact with the same inner contact area but deeper fusion zone can result in substantially lower total contact resistances because the area of the LFC/wafer interface for a three-dimensional contact will be greater with larger melt depths. For example, an LFC with an 80 μm inner contact area produced with a 50 μm beam results in a deeper doped region and a total contact resistance of approximately 300 Ω versus 450 Ω when produced using a 70 μm beam.

(iv) Processing with the laser conditions considered in this study leads to the formation of a central peak region and significant molten pool surface deformation, particularly at higher power density levels. The formation of these features does not seem to impact total contact resistance, which is primarily influenced by the interfacial contact area of the resolidified Al–Si fusion zone.

## ACKNOWLEDGEMENTS

The authors would like to thank Joshua Yearsley, Dr. Josh Stapleton, Dr. Trevor Clark, and Julie Anderson for assistance with sample preparation and LFC characterization. The authors also acknowledge Dr. Brian Downey for providing support with the SENTAURUS simulations. The authors also thank the American Welding Society for a Graduate Student Research Fellowship and BP Solar for additional support. K. C. Kragh-Buetow is supported by a NASA Space Technology Research Fellowship.

## REFERENCES

1. Canizo C, Coso G, Sinke WC. Crystalline silicon solar module technology: towards the 1€ per watt-peak goal. *Progress in Photovoltaics* 2009; **17**: 199–209. DOI: 10.1002/pip.878
2. Chopra KL, Paulson PD, Dutta V. Thin film solar cells: an overview. *Progress in Photovoltaics* 2004; **12**: 69–92. DOI: 10.1002/pip.541
3. Wang S, Lennon A, Tjahjono B, Mai L, Vogl B, Wenham S. Overcoming over-plating problems for PECVD SiNx passivated laser doped p-type multicrystalline silicon solar cells. *Solar energy materials and solar cell* 2012; **99**: 226–234. DOI: 10.1016/j.solmat.2011.12.003
4. Blecher JJ, Palmer TA, DebRoy T. Laser-silicon interaction for selective emitter formation in photovoltaics. I. Numerical model and validation. *Journal of Applied Physics* 2012; **112**(11). DOI: 10.1063/1.4768531
5. Schneiderlochner E, Preu R, Ludemann R, Glunz SW. Laser-fired rear contacts for crystalline silicon solar cells. *Progress in Photovoltaics* 2002; **10**: 29–34. DOI: 10.1002/pip.422
6. Schultz O, Glunz SW, Willeke GP. Multicrystalline silicon solar cells exceeding 20% efficiency. *Progress in Photovoltaics* 2004; **12**(7): 553–558. DOI: 10.1002/pip.583
7. Raghavan A, Palmer TA, DebRoy T. Evolution of laser-fired aluminum-silicon contact geometry in photovoltaic devices. *Journal of Applied Physics* 2012; **111**(2). DOI: 10.1063/1.3675442
8. Kray D, Glunz S. Investigation of laser-fired rear-side recombination properties using an analytical model. *Progress in Photovoltaics* 2006; **14**(3): 195–201. DOI: 10.1002/pip.660
9. Wolf A, Biro D, Nekarda J, Stumpp S, Kimmerle A, Mack S, Preu R. Comprehensive analytical model for locally contacted rear surface passivated solar cells. *Journal of Applied Physics* 2010; 108. DOI: 10.1063/1.3506706
10. Mueller J Bothe K Gatz S, Haase F, Mader C, Brendel R. Recombination at laser-processed local base contacts by dynamic infrared lifetime mapping. *Journal of Applied Physics* 2010; 108. DOI: 10.1063/1.3517109
11. Tucci M, Talgorn E, Serenelli L, Salza E, Izzi M, Mangiapane P. Laser fired back contact for silicon solar cells. *Thin Solid Films* 2008; **516**: 6767–6770. DOI: 10.1016/j.tsf.2007.12.079
12. Schneiderlochner E, Grohe A, Ballif C, Glunz SW, Preu R, Willeke G. Investigations on laser-fired contacts for passivated rear solar cells, IEEE Photovoltaic Specialists Conference 2002; 0-7803-7471-1, pp. 300–303.
13. Brendle W, Nguyen VX, Grohe A, Schneiderlochner E, Rau U, Palfinger G, Werner JH. $20 \cdot 5\%$ efficient silicon solar cell with a low temperature rear side process using laser-fired contacts. *Progress in Photovoltaics* 2006; **14**: 653–662. DOI: 10.1002/pip.696
14. Zastrow U, Houben L, Meertens D, Grohe A, Brammer T, Schneiderlochner E. Characterization of laser-fired contacts in PERC solar cells: SIMS and TEM analysis applying advanced preparation techniques. *Applied Surface Science* 2006; **252**(19): 7082–7085. DOI: 10.1016/j.apsusc.2006.02.114
15. Van Kerschaver E, Beaucarne G. Back-contact solar cells: a review. *Progress in Photovoltaics* 2006; **14**: 107–123. DOI: 10.1002/pip.657
16. Fischer B. Loss analysis of crystalline silicon solar cells using photoconductance and quantum efficiency

measurements, Dissertation, Universitat Konstanz, 2003.
17. Ortega P, Orphella A, Martin I, Colina M, Lopez G, Voz C, Sanchez MI, Molpeceres C, Alcubilla R. Laser-fired contact optimization in c-Si solar cell. *Progress in Photovoltaics* 2012; **20**(2): 173–180. DOI: 10.1002/pip.1115
18. Martin I, Labrune M, Salomon A, Roca i Cabarrocasb P, Alcubilla R. Laser fired contacts applied to the rear surface of heterojunction silicon solar cells. *Solar Energy Materials and Solar Cells* 2011: **95**(11): 3119–3123. DOI: 10.1016/j.solmat.2011.06.049
19. Glunz SW, Schneiderlochner E, Kray D, Grohe A, Hermle M, Kampwerth H, Preu R, Willeke G. Laser fired contact silicon solar cells on p- and n-substrates, Proceedings of the 19th EU PVSEC, Paris, France 2004; 408–411.
20. Zhou Y. *Microjoining and Nanojoining*. Woodhead Publishing: England, 2008.
21. He X, DebRoy T, Fuerschbach PW. Alloying element vaporization during laser spot welding of stainless steel. *Journal of Physics D: Applied Physics* 2003; **36**: 3079–3088. DOI: 10.1088/0022-3727/36/23/033
22. Cunningham DW. BP Solar International, reaching grid parity using BP solar crystalline silicon technology: a systems class application, DOE Award Number: DE-FC36-07GO17049.006.
23. Decesar B. Investigation of process parameter optimization of laser-fired back contact silicon solar cells, MS Thesis Penn State University, 2010.
24. Hedrick B. Characterization of laser fired contacts laser doped emitters and fixed charge passivation for improved silicon solar cells, MS Thesis Penn State University, 2011.
25. Hua Z. Beam delivery system for laser fired contacts, MS Thesis Penn State University, 2010.
26. Hua Z, Reutzel EW, Zou L. Beam delivery techniques for laser fired contacts, ICALEO 2010, #M1101.
27. Schutz V, Horn A, Stute U. High-throughput process parallelization for laser surface modification on Si-solar cells: determination of the process window. *Proceedings of SPIE* 2012; Article number: 82440X. DOI: 10.1117/12.907972
28. Semak VV, Knorovsky GA, MacCallum DO, Roach RA. Effect of surface tension on melt pool dynamics during laser pulse interaction. *Journal of Physics D: Applied Physics* 2006; **39**: 590–595. DOI: 10.1088/0022-3727/39/3/025
29. Bennett TD, Krajnovich DJ, Grigoropoulos CP, Baumgart P, Tam AC. Marangoni mechanism in pulsed laser texturing of magnetic disk substrates. *Journal of Heat Transfer* 1991; **119**: 589–596. DOI: 10.1115/1.2824146
30. Cho J-H, Farson DF, Milewski JO, Hollis KJ. Weld pool flows during initial stages of keyhole formation in laser welding. *Journal of Physics D: Applied Physics* 2009; **42**. DOI: 10.1088/0022-3727/42/17/175502
31. Cox RH, Strack H. Ohmic contacts for GaAs devices. *Solid State Electronics* 1967; **10**: 1213–1218. DOI: 10.1016/0038-1101(67)90063-9
32. Hara T, Suzuki H, Furukawa M, Ameyiya K. Contact resistance of Al/Si ohmic electrodes formed by rapid lamp sintering. *Japanese Journal of Applied Physics* 1983; **22**(6): L340–L342. DOI: 10.1143/JJAP.22.L340
33. Hovington P, Dominique D, Gauvin R. CASINO: A new Monte Carlo code in C language for electron beam interaction—part I: description of the program. *Scanning* 1997; **19**(1): 1–14. DOI: 10.1002/sca.4950190101
34. Blecher JJ, Palmer TA, Reutzel EW, DebRoy T, Laser-silicon interaction for selective emitter formation in photovoltaics. II. Model applications. *Journal of Applied Physics* 2012; 112, DOI: 10.1063/1.4768540.
35. He X, Elmer JW, DebRoy T. Heat transfer and fluid flow in laser microwelding. *Journal of Applied Physics* 2007; **97**. DOI: 10.1063/1.1873032
36. David SA, Vitek JM. Correlation between solidification parameters and weld microstructures. *International Materials Review* 1989; **34**: 213–245.
37. Sze, SM, Ng KK. *Physics of Semiconductor Devices*, 3rd edn. John Wiley & Sons: Hoboken, NJ, 2007.
38. Trumbore FA. Solid solubilities of impurity elements in germanium and silicon. *The Bell System Technical Journal* 1960; **39**(1): 205–233.